

Cite this article as: Zhao Tianli, Zhang Bing, Zhang Zhijuan, et al. Flow Stress Prediction for Ti/Ni/Ti Laminated Composites During Hot Compressing[J]. Rare Metal Materials and Engineering, 2022, 51(10): 3663-3678.

ARTICLE

Flow Stress Prediction for Ti/Ni/Ti Laminated Composites During Hot Compressing

Zhao Tianli¹, Zhang Bing^{1,2}, Zhang Zhijuan¹, Ma Yanheng¹, Dang Xiaohan¹, Cai Jun^{1,2}

¹ College of Metallurgy Engineering, Xi'an University of Architecture and Technology, Xi'an 710055, China; ² National & Local Engineering Researching Center for Functional Materials Processing, Xi'an 710055, China

Abstract: In order to establish a constitutive equation which can reasonably describe the Ti/Ni/Ti laminated composites process, the hot deformation behavior of Ti/Ni/Ti laminated composite during the bonding process was studied on Gleeble-3500 thermo-mechanical simulator at the temperature of 550~850 °C, strain rate of 0.001~1 s⁻¹, and deformation of 65%. Four constitutive models, including modified Johnson-Cook (MJC) model, strain compensated Arrhenius (SCA) model, multivariate nonlinear regression (DMNR) model, and modified Inoue Sin (MIS) model were used to predict the elevated temperature flow behavior of laminated composite. A comparative research on the experimental values and the predicted values of the four models was conducted. Besides, the accuracy of the average absolute relative error (AARE), correlation coefficient (*R*) and the relative error was compared to confirm the reasonability of these four models. Results show that the MJC, DMNR and MIS model are not suitable for the description of flow behavior of Ti/Ni/Ti laminated composites, while the predicted values of SCA model agree well with the experimental values except under some deformation conditions.

Key words: Ti/Ni/Ti laminated composites; hot compression; flow stress; constitutive equation

Ti/Ni composite owns the advantages of pure titanium with low density, high specific strength and strong corrosion resistance, and the characteristics of pure nickel with high conductivity and thermal conductivity, strong toughness and good plastic processing, which is widely used in various fields^[1,2]. So, it has attracted more and more attention recently.

Ti/Ni laminated composite consists of Ti (hcp) and Ni (fcc) with different crystal structure, which results in different deformation mechanisms and deformation behavior of the constituent layers during the roll bonding processing. Moreover, due to the existence of the interface, the stress state of the constituent layer changes during the rolling bonding processing, resulting in the change of stress, the deformation behavior, the deformation mechanism and the interface bonding status. So, it is very important to analyze the deformation behavior of Ti/Ni laminated composite.

With the development of numerical simulation methods, the finite element method has been widely used in optimization of thermal processing parameters and the analysis of metal

forming processes^[3,4]. The flow behavior of the material can be represented by the constitutive equation, while the constitutive equations are served as an input condition usually, which represent the connection between flow stress and deformation conditions (strain, strain rate, and deformation temperature) by numerical simulations. Thus, the accuracy of the simulation results depends strongly on the accuracy of the constitutive equation. At present, research on the hot deformation behavior of materials through hot compression has mainly focused on pure metals^[5], alloys^[6-8], and particle-reinforced metal matrix composites^[9,10], while less on layered structural composites. This is due to the existence of the interface that makes the prediction of the constitutive equation on deformation behavior difficult. In addition, the existing constitutive equations have seldom been compared to investigate which is more suitable for describing bonding process of the layered structure composite. Therefore, the comparative investigation of constitutive equations for laminated composites under different deformation conditions

Received date: October 29, 2021

Foundation item: National Natural Science Foundation of China (51874226)

Corresponding author: Zhang Bing, Ph. D., Professor, College of Metallurgy Engineering, Xi'an University of Architecture and Technology, Xi'an 710055, P. R. China, E-mail: r.zhang1112@163.com

Copyright © 2022, Northwest Institute for Nonferrous Metal Research. Published by Science Press. All rights reserved.

is necessary, which is contributed to identify more reasonable input conditions for the numerical simulation.

According to the difference of parameters in the constitutive model, it can be roughly divided into three categories: phenomenological constitutive model, kinetic constitutive model and physical constitutive model. The phenomenological constitutive model describes flow stresses based on empirical formulas, and the parameters in the functions usually have no explicit physical significance. The common phenomenological constitutive model is the Johnson-Cook (JC) constitutive model, and the strong applicability of the JC constitutive model is that some corrections according to the material characteristics based on the original model can significantly improve the solution accuracy of the equation^[11,12]. However, this constitutive model ignores the mutual effects of the influencing factors on the flow stresses, which may reduce the accuracy of the constitutive equations^[13]. Later, Lin^[14] et al proposed a modified JC constitutive model to compensate for the shortcomings of the original JC model. The Arrhenius constitutive model belongs to the kinetic constitutive model, which mostly reflects the relationship of the steady-state stress or peak stress and the deformation parameters, while ignoring the influence of the strain. Researchers have put great efforts to correct this equation, using strain compensation parameters to predict the flow stress of metal materials, such as GH4169^[15], 42CrMo steel^[16] and Inconel718 high-temperature alloy^[17]. The multivariate nonlinear regression (DMNR) model is a scattering map based on test data and does not require a specific constitutive model, which takes into account the individual effect of temperature, strain rate and strain on stress, and the interaction between them. Physics-based models can more accurately represent deformation behavior in a wide range of temperatures and strain rates, which are not always preferred because physics-based models contain a large number of material constants that may not be involved by empirical-based models. The Inoue Sin constitutive model belongs to an empirical model. The impact of the deformation degree on the flow stress is considered in the typical Inoue Sin constitutive model, while it fails to show the trend of the flow stress curve of the material at different temperatures. So, it is necessary to correct to make it more consistent with the rheological characteristics of the material under different working conditions.

In this study, hot compression tests of Ti/Ni/Ti laminated composites were carried out in the temperature range of 550~850 °C, strain rate range of 0.001~1 s⁻¹, and deformation of 65%. The hot deformation behavior of Ti/Ni/Ti laminated composite was studied by analyzing the true stress-true strain curve. And then the modified JC constitutive model, strain compensated Arrhenius constitutive model, multivariate nonlinear regression constitutive model and modified Inoue Sin constitutive model were established to compare the accuracy of the constitutive equations. Finally, the applicability of these four models was evaluated by average absolute relative error (AARE), correlation coefficient (*R*) and relative error.

1 Experiment

The raw materials were TA1 and N6 plate after full annealing with dimensions of 100 mm×150 mm×3.0 mm and 100 mm×150 mm×6.0 mm, respectively. The chemical compositions and microscopic structure of raw materials are listed in Table 1 and Fig.1, respectively. TA1 is characterized by uniform recrystallized grains, and N6 has uneven grains with a little annealing twin crystal.

The hot compression tests mainly adopted the cylindrical samples with $\Phi 8$ mm×3 mm (TA1) and $\Phi 8$ mm×6 mm (N6), which were cut from the raw materials. All the contact surfaces of TA1 and N6 were polished with 1000# sandpaper and treated by ultrasonic cleaning with alcohol, and then the specimens were stacked to TA1-N6-TA1, with total thickness of 12 mm, as illustrated in Fig.2. A thermal couple spot was welded to the center region of the N6 specimen surface. The graphite foils were imposed between the specimen and the anvil to decrease the friction. Then the stacked samples were put in the thermal compression equipment to heat up to experimental temperature at heating rate of 10 °C/s and held for 7 min to guarantee a homogeneous temperature distribution of the specimen, as illustrated in Fig. 3. Compression tests were made in the temperature and strain rate range of 550~850 °C with 50 °C intervals and 0.001~1 s⁻¹. The samples were deformed later to a true compression strain

Table 1 Chemical composition of TA1 and N6 (wt%)

	Fe	C	Si	N	H	O	Ti
TA1	0.15	0.05	0.1	0.03	0.015	0.15	Bal.
	Cu	Fe	Mn	C	Si	S	Ni+Co
N6	≤0.06	≤0.1	≤0.05	≤0.1	≤0.1	≤0.005	≥99.5

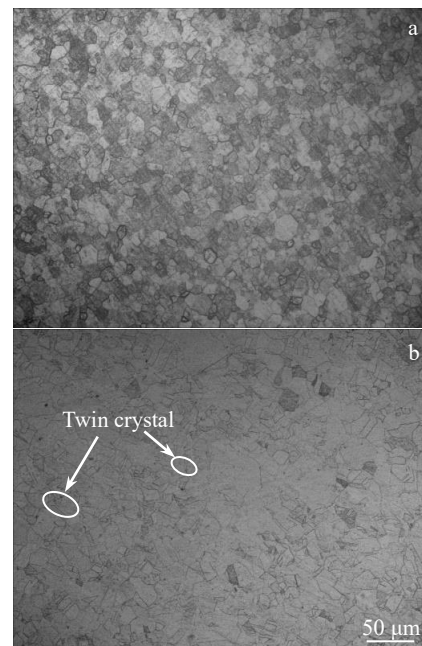


Fig.1 Microstructures of raw materials of TA1 (a) and N6 (b)

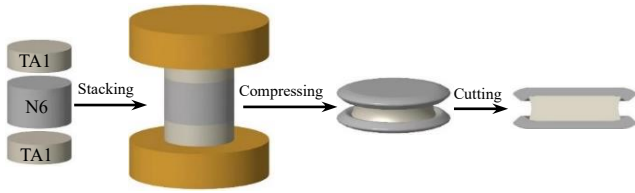


Fig.2 Process route of the hot compression test

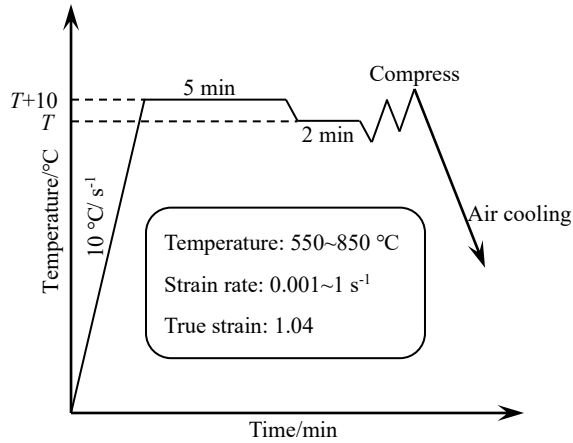


Fig.3 Parameters of the hot compression test

of 1.04. Afterwards, it was cooled in air. The stress-strain curves were automatically recorded in the hot compression process through the Gleeble-3500 thermal simulator system.

2 Results

2.1 True stress-strain curves

Fig.4 shows the flow stress-strain curves of TA1/N6/TA1

laminated composites in temperature range of 550~850 °C, and strain rate range of 0.001~1s⁻¹ during hot compression procession, which reflects the influence of the deformation temperature, the strain rate and the deformation degree on the high temperature deformation behavior of the TA1/N6/TA1 laminated composites. According to the figure, the laminated composites have the following characters.

(1) The flow stress of the composite decreases with increasing the deformation temperature and decreasing the strain rate, showing positive strain rate sensitivity and negative temperature sensitivity. This is because both TA1 and N6 are positive strain rate sensitive materials and negative temperature sensitive materials.

(2) The flow stress of the composite reaches the peak rapidly with increasing the temperature or decreasing the strain rate. However, the strain corresponding to the peak stress is increased compared with the traditional materials due to the presence of the bonding interface, the asynchronism of deformation and the coordination of deformation between each other.

(3) Composites under almost all deformation conditions show the steady-state flow characteristics. That is, when the true strain exceeds a certain value, the true stress changes little with the increase of strain. It shows that the constitute layer is stable during deformation, and the softening caused by dynamic recrystallization and strain hardening almost reach the dynamic equilibrium. This is because the interface of composite combines well and the deformation of each constitute layer is uniform, and the mutual coordination between composition layers is better.

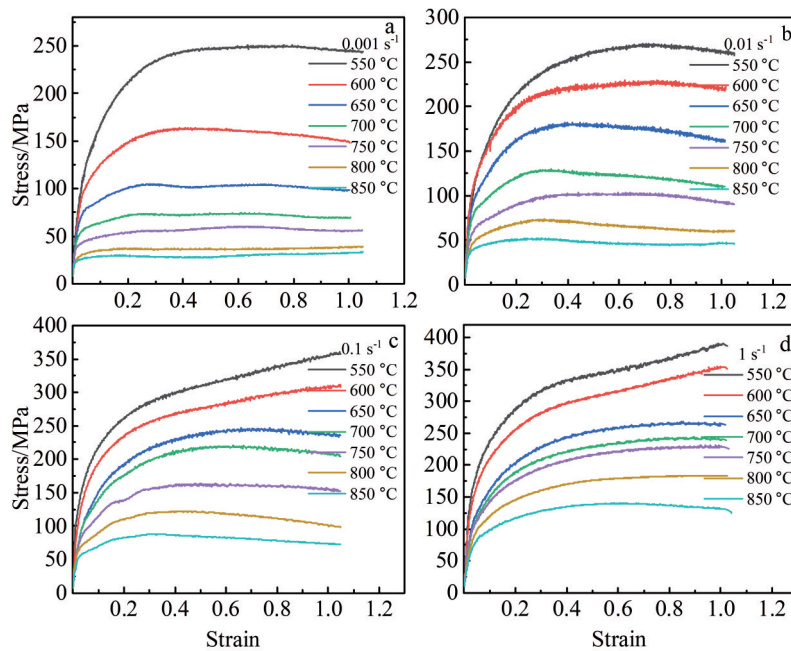


Fig.4 True stress-true strain curves of TA1/N6/TA1 laminated composites at different strain rates: (a) 0.001 s⁻¹, (b) 0.01 s⁻¹, (c) 0.1 s⁻¹, and (d) 1 s⁻¹

(4) The strain rate is sensitive to the deformation required for the composites to enter the steady flow stage. When the strain rate is lower than 0.1 s^{-1} , the composites enter into the steady-state rheological stage with small deformation. While, as the strain rate is higher than 0.1 s^{-1} , the degree of deformation required for the composite to enter into the steady flow stage is related to temperature. When the deformation temperature is higher than $650 \text{ }^\circ\text{C}$, due to the compensation of deformation temperature on strain rate, the material can enter into the steady flow stage as soon as possible, but when the deformation temperature is lower than $650 \text{ }^\circ\text{C}$, the degree of deformation required for the material to enter into the steady flow stage is large.

2.2 Macroscopic structure

Fig. 5 shows the macroscopic structures of TA1/N6/TA1 laminated composites under the deformation temperature of $550\sim 850 \text{ }^\circ\text{C}$ and strain rate of $0.001\sim 1 \text{ s}^{-1}$. The TA1 layers are extruded from the laminate with the increase of temperature. This is due to the softening of the titanium layer and the equivalent stress behavior of laminate in which each constituent layer is subjected to the same stress^[18]. The deformation degree of titanium layer increases with the increase of deformation temperature at the same strain rate, and it is easier for the flow stress of the composite to reach a stable state (as shown in Fig. 4). It can also be seen that the higher the temperature, the larger the deformation degree of nickel with the increase of strain rate.

2.3 Modified Johnson-Cook (MJC) model

The modified Johnson-Cook (MJC) model has been proposed as^[19-21]:

$$\sigma = (A_1 + B_1\varepsilon + B_2\varepsilon^2 + B_3\varepsilon^3) (1 + C_1 \ln \dot{\varepsilon}^* + C_2 \ln \dot{\varepsilon}^{*2} + C_3 \ln \dot{\varepsilon}^{*3}) \times \exp[(\lambda_1 + \lambda_2 \ln \dot{\varepsilon}^* + \lambda_3 \ln \dot{\varepsilon}^{*2} + \lambda_4 \ln \dot{\varepsilon}^{*3})T^*] \quad (1)$$

where $\dot{\varepsilon}^* = \dot{\varepsilon}/\dot{\varepsilon}_0$ is a dimensionless strain rate ($\dot{\varepsilon}$ and $\dot{\varepsilon}_0$ are the strain rate (s^{-1}) and the reference strain rate (s^{-1}), respectively); $A_1, B_1, B_2, B_3, C_1, C_2, C_3, \lambda_1, \lambda_2, \lambda_3$ and λ_4 are the materials constants. The T^* can be expressed as Eq.(2):

$$T^* = T - T_{\text{ref}} \quad (2)$$

where T_{ref} is the reference temperature. Herein, 1 s^{-1} and 823 K have been set as the reference strain rate and reference temperature in this model, respectively, and then Eq.(1) can be expressed as

$$\sigma = A_1 + B_1\varepsilon + B_2\varepsilon^2 + B_3\varepsilon^3 \quad (3)$$

Taking the corresponding experimental stress values and strain into Eq.(3), the relation between ε and σ is obtained as



Fig.5 Macroscopic structures of TA1/N6/TA1 laminated composite under different conditions

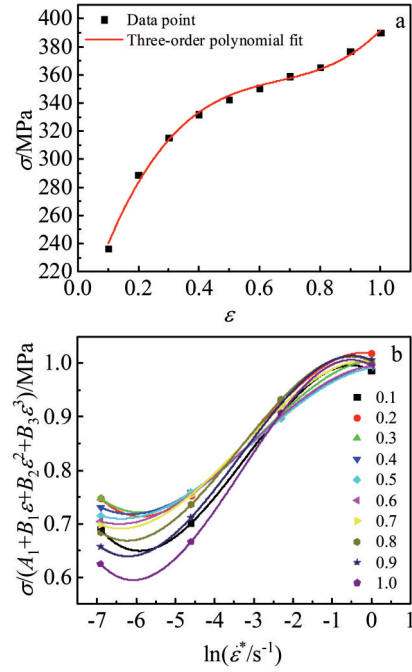


Fig.6 Relation of σ - ε at $823 \text{ K}/1 \text{ s}^{-1}$ (a) and $\sigma/(A_1 + B_1\varepsilon + B_2\varepsilon^2 + B_3\varepsilon^3) - \ln \dot{\varepsilon}^*$ at 823 K (b)

shown in Fig.6a, and then the data points in the figure in three curves are fitted to obtain the values of A_1, B_1, B_2 and B_3 , where $A_1=179.384, B_1=695.671, B_2=-972.713$ and $B_3=489.417$.

When the deformation temperature is the reference temperature, Eq.(1) can be expressed as:

$$\sigma = (A_1 + B_1\varepsilon + B_2\varepsilon^2 + B_3\varepsilon^3) (1 + C_1 \ln \dot{\varepsilon}^* + C_2 \ln \dot{\varepsilon}^{*2} + C_3 \ln \dot{\varepsilon}^{*3}) \quad (4)$$

The value of C_1, C_2, C_3 can be obtained from $\sigma/(A_1 + B_1\varepsilon + B_2\varepsilon^2 + B_3\varepsilon^3) - \ln \dot{\varepsilon}^*$ plot as shown in Fig. 6b, where $C_1=-0.01410, C_2=-0.03003, C_3=-0.00314$.

To reduce the computation and complexity, a new parameter λ is introduced, which is expressed as:

$$\lambda = \lambda_1 + \lambda_2 \ln \dot{\varepsilon}^* + \lambda_3 \ln \dot{\varepsilon}^{*2} + \lambda_4 \ln \dot{\varepsilon}^{*3} \quad (5)$$

So, Eq.(1) can be written as follows:

$$\frac{\sigma}{(A_1 + B_1\varepsilon + B_2\varepsilon^2 + B_3\varepsilon^3) (1 + C_1 \ln \dot{\varepsilon}^* + C_2 \ln \dot{\varepsilon}^{*2} + C_3 \ln \dot{\varepsilon}^{*3})} = e^{\lambda T^*} \quad (6)$$

Take the natural logarithms at both sides of the upper equation:

$$\ln \left[\frac{\sigma}{(A_1 + B_1\varepsilon + B_2\varepsilon^2 + B_3\varepsilon^3) (1 + C_1 \ln \dot{\varepsilon}^* + C_2 \ln \dot{\varepsilon}^{*2} + C_3 \ln \dot{\varepsilon}^{*3})} \right] = \lambda T^* \quad (7)$$

Take the true strain of 0.1 as an example, as shown in Fig.7a. According to Eq.(5), the value of $\lambda_1, \lambda_2, \lambda_3$ and λ_4 can be obtained by the relation of $\lambda - \ln \dot{\varepsilon}^*$, as shown in Fig.7b.

Table 2 presents the parameters of the MJC model for Ti/Ni/Ti laminated composites.

The MJC constitutive equation can be generated, which is listed below:

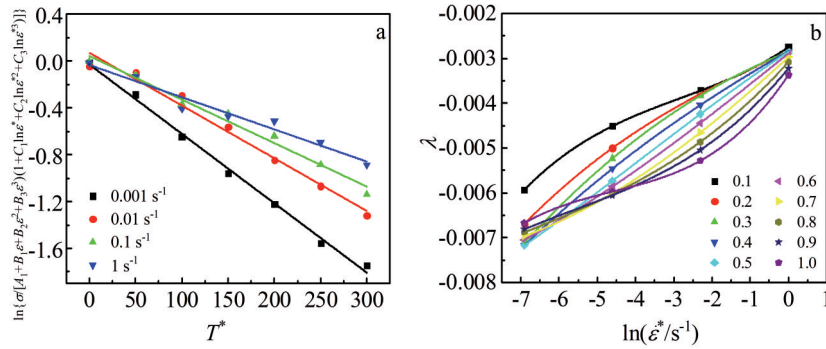


Fig.7 Relation of $\ln \left[\frac{\sigma}{(A_1 + B_1 \varepsilon + B_2 \varepsilon^2 + B_3 \varepsilon^3)(1 + C_1 \ln \dot{\varepsilon}^* + C_2 \ln \dot{\varepsilon}^{*2} + C_3 \ln \dot{\varepsilon}^{*3})} - T^* \right]$ (a) and $\lambda - \ln \dot{\varepsilon}^*$ (b)

Table 2 Parameters of the MJC model

Parameter	A_1	B_1	B_2	B_3	C_1	C_2	C_3	λ_1	λ_2	λ_3	λ_4
Value	179.4	695.7	-973	489.4	-0.014	-0.03	-0.003	-0.003	0.00071	4.86×10^{-6}	3.95×10^{-6}

$$\sigma = (179.4 + 695.7\varepsilon - 972.7\varepsilon^2 + 489.4\varepsilon^3) \times (1 - 0.014\ln\dot{\varepsilon}^* - 0.03\ln\dot{\varepsilon}^{*2} - 0.003\ln\dot{\varepsilon}^{*3}) \times \exp\left[(-0.003 + 0.00071\ln\dot{\varepsilon}^* + 4.86 \times 10^{-5} \ln\dot{\varepsilon}^{*2} + 3.95 \times 10^{-6} \ln\dot{\varepsilon}^{*3})T^*\right] \quad (8)$$

It is observed from Fig.8 that the predicted stress values are in good agreement with experimental stress value at temperature of 650~850 °C or strain rate of 0.1~1 s⁻¹. While under other conditions, the predicted value is somewhat deviated from the experimental value.

2.4 Strain compensated Arrhenius (SCA) model

Generally speaking, the hot deformation behavior of materials is a process of thermal activation, and the effects of deformation temperature and strain rate on flow stress can be

expressed by Arrhenius equation:

$$\dot{\varepsilon} = AF(\sigma) \exp\left(-\frac{Q}{RT}\right) \quad (9)$$

where $F(\sigma)$ is the function of true stress. Taking the function into Eq.(9), then the following relations can be obtained.

$$\dot{\varepsilon} = A_1 \sigma^{n_1} \exp\left(-\frac{Q}{RT}\right) \quad \alpha\sigma < 0.8 \quad (10)$$

$$\dot{\varepsilon} = A_2 \exp(\beta\sigma) \exp\left(-\frac{Q}{RT}\right) \quad \alpha\sigma > 1.2 \quad (11)$$

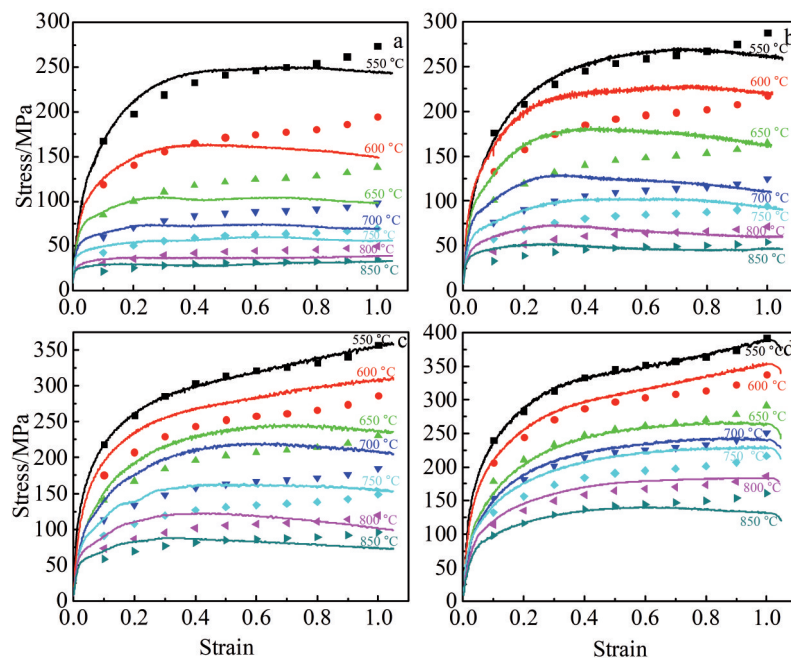


Fig.8 Comparison between experimental and predicted flow stress by MJC model at different strain rates: (a) 0.001 s⁻¹, (b) 0.01 s⁻¹, (c) 0.1 s⁻¹, and (d) 1 s⁻¹

$$\dot{\epsilon} = A [\sinh(\alpha\sigma)]^n \exp\left(-\frac{Q}{RT}\right) \quad \text{for all } \sigma \quad (12)$$

where Q is the activation energy of deformation (J/mol); R is the constant of gas ($8.314 \text{ J}\cdot\text{mol}^{-1}\cdot\text{K}^{-1}$); A , A_1 , A_2 , n , β , α and n_1 are the material constants and $\alpha = \beta/n_1$. In general, Eq.(10) is applicable to the thermal deformation process with low flow stress, exponential Eq. (11) is applicable to the thermal deformation process with high flow stress, and hyperbolic sine Eq.(12) is applicable to both cases.

Both sides of Eq.(10) and Eq.(11) are taken in the natural logarithms, and the following equations can be obtained.

$$\ln \dot{\epsilon} = \ln A_1 + n_1 \ln \sigma - \frac{Q}{RT} \quad (13)$$

$$\ln \dot{\epsilon} = \ln A_2 + \beta\sigma - \frac{Q}{RT} \quad (14)$$

The values of the flow stress and corresponding strain rate under different strain are substituted into Eq.(13) and Eq.(14). The values of n_1 and β can be obtained from the slopes of the lines in the $\ln\sigma$ - $\ln\dot{\epsilon}$ and σ - $\ln\dot{\epsilon}$ plots, respectively. Then, the value of $\alpha = \beta/n_1$ can be obtained. Take the strain of 0.1 for example, as presented in Fig.9a and Fig.7b. The values of n_1 , β and α are obtained, where $n_1 = 8.2365$, $\beta = 0.0842$, $\alpha = 0.010224$.

Taking the natural logarithm of both sides of Eq.(12):

$$\ln \dot{\epsilon} = \ln A + n \ln [\sinh(\alpha\sigma)] - \frac{Q}{RT} \quad (15)$$

Taking the partial differential score of Eq.(15):

$$Q = R \left| \frac{\partial \ln \dot{\epsilon}}{\partial \ln [\sinh(\alpha\sigma)]} \right|_T \left| \frac{\partial \ln [\sinh(\alpha\sigma)]}{\partial (1/T)} \right|_{\dot{\epsilon}} \quad (16)$$

Taking $\left| \frac{\partial \ln \dot{\epsilon}}{\partial \ln [\sinh(\alpha\sigma)]} \right|_T$ as n , $\left| \frac{\partial \ln [\sinh(\alpha\sigma)]}{\partial (1/T)} \right|_{\dot{\epsilon}}$ as m .

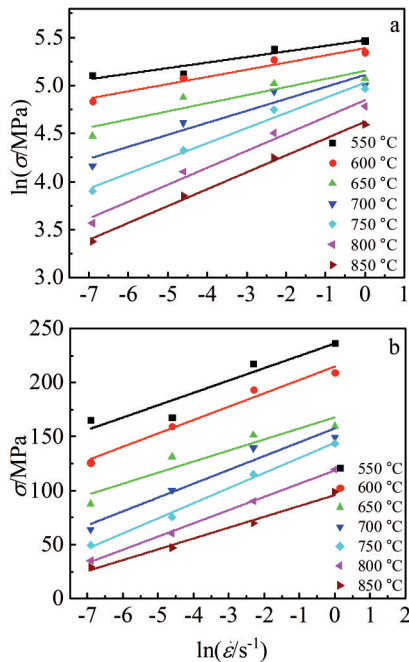


Fig.9 Relation of $\ln\sigma$ - $\ln\dot{\epsilon}$ (a) and σ - $\ln\dot{\epsilon}$ (b)

The value of material constant n and m can be obtained from the slopes of the lines of $\ln[\sinh(\alpha\sigma)]$ - $\ln\dot{\epsilon}$ and $\ln[\sinh(\alpha\sigma)]$ - $1/T$ at a particular temperature and strain, respectively. The mean value of n and m are set as the final value of n and m . Take the strain of 0.1 for example, as presented in Fig.10a and 10b. The values of n and m are obtained, where $n=6.0578$, $m=5.5430$, then $Q=279.1682 \text{ kJ/mol}$.

The effects of the temperature and strain rate on the thermal deformation behavior of the material can be expressed in terms of the Zener-Holloman parameter, as expressed in Eq. (17)^[21-27]. Take Eq.(17) into Eq.(12) to obtain another form of the Zener-Holloman parameter as shown in Eq.(18).

$$Z = \dot{\epsilon} \exp\left(\frac{Q}{RT}\right) \quad (17)$$

$$Z = A \ln [\sinh(\alpha\sigma)]^n \quad (18)$$

Taking the natural logarithm of both sides of Eq.(18):

$$\ln Z = n \ln [\sinh(\alpha\sigma)] + \ln A \quad (19)$$

The values of $\ln A$ and n can be determined from the intercept and slope of $\ln Z$ - $\ln[\sinh(\alpha\sigma)]$ plot at a particular strain. Take the strain of 0.1 for example as presented in Fig. 11. The values of $\ln A$ and n are obtained, where $\ln A = 29.2564$, $n = 5.8789$.

From the above calculations, the parameters of constitutive model under the entire true strain are shown in Table 3.

It can be seen that the material parameters vary with the strain. So, considering the strain effect on the material parameters, polynomial is used to compensate the strain of α , Q , n and $\ln A$ ^[28,29]. The appropriate polynomial is selected as Eq. (20). It has been found that there is an eight-order polynomial to represent the influence of strain on material parameters with a good correlation, as shown in Fig.12.

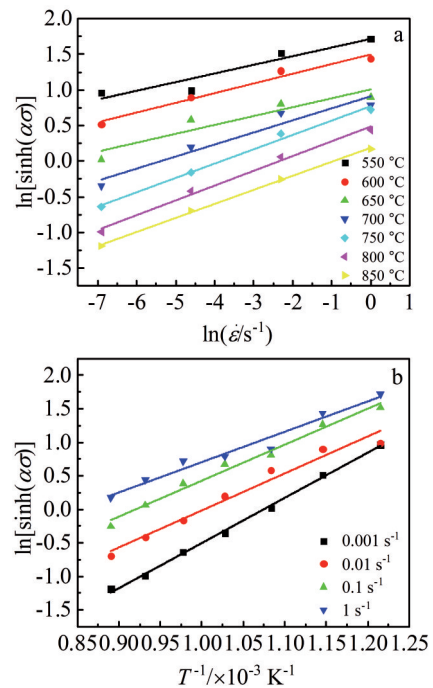


Fig.10 Relation of $\ln[\sinh(\alpha\sigma)]$ - $\ln\dot{\epsilon}$ (a) and $\ln[\sinh(\alpha\sigma)]$ - $1/T$ (b)

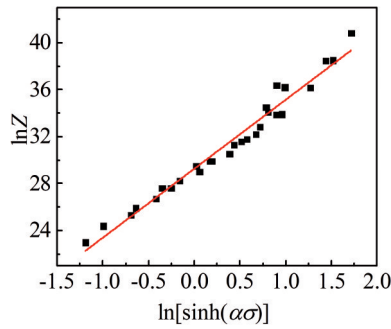


Fig.11 Relation between lnZ and ln[sinh(alpha*sigma)]

Table 3 Parameters of TA1/N6/TA1 laminated composites

ϵ	α	Q	$\ln A$	n
0.1	0.010 224	279.168 2	29.256 44	5.878 87
0.2	0.008 824	275.797 8	28.758 93	5.258 92
0.3	0.008 292	265.947	27.576 42	4.839 78
0.4	0.007 96	258.564 4	26.801 32	4.613 47
0.8	0.007 74	256.022	26.496 37	4.584 88
0.6	0.007 544	254.710 2	26.455 23	4.481 12
0.7	0.007 404	255.430 9	26.759 77	4.414 12
0.8	0.007 309	254.439 2	26.759 27	4.369 25
0.9	0.007 218	251.768 1	26.561 67	4.284 37
1	0.007 103	251.613 7	26.683 69	4.261 48

$$\begin{aligned} \alpha &= D_0 + D_1 \epsilon + D_2 \epsilon^2 + D_3 \epsilon^3 + D_4 \epsilon^4 + D_5 \epsilon^5 + D_6 \epsilon^6 + D_7 \epsilon^7 + D_8 \epsilon^8 \\ Q &= F_0 + F_1 \epsilon + F_2 \epsilon^2 + F_3 \epsilon^3 + F_4 \epsilon^4 + F_5 \epsilon^5 + F_6 \epsilon^6 + F_7 \epsilon^7 + F_8 \epsilon^8 \\ \ln A &= C_0 + C_1 \epsilon + C_2 \epsilon^2 + C_3 \epsilon^3 + C_4 \epsilon^4 + C_5 \epsilon^5 + C_6 \epsilon^6 + C_7 \epsilon^7 + C_8 \epsilon^8 \\ n &= E_0 + E_1 \epsilon + E_2 \epsilon^2 + E_3 \epsilon^3 + E_4 \epsilon^4 + E_5 \epsilon^5 + E_6 \epsilon^6 + E_7 \epsilon^7 + E_8 \epsilon^8 \end{aligned} \quad (20)$$

Polynomial fitting results for α , Q , n and $\ln A$ are provided in Table 4.

Substituting Eq. (18) into Eq. (12) to obtain the function equation of the rheological stress about the Z value:

$$\sigma = \frac{1}{\alpha} \ln \left\{ \left(\frac{Z}{A} \right)^{\frac{1}{n}} + \left[\left(\frac{Z}{A} \right)^{\frac{2}{n}} + 1 \right]^{\frac{1}{2}} \right\} \quad (21)$$

According to Eq. (21), the flow stress under a particular strain can be predicted, where $Z = \dot{\epsilon} \exp(Q/RT)$.

It is observed from Fig. 13 that the deviation is larger

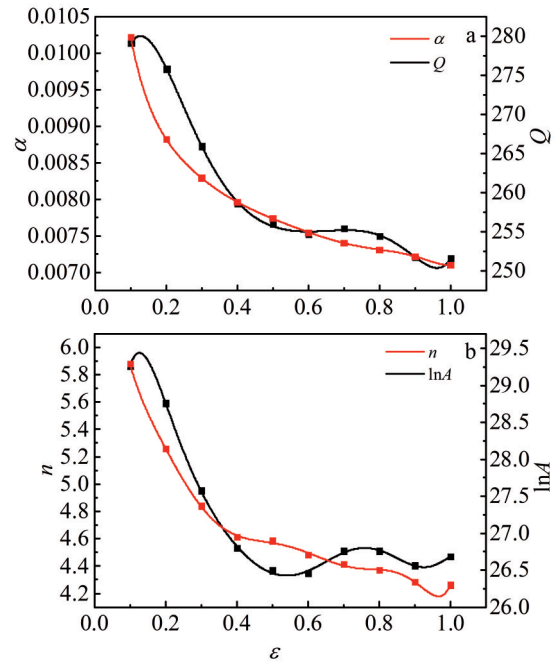


Fig.12 Eight-order polynomial fitting with different parameters: (a) α and Q ; (b) n and $\ln A$

compared with the experimental value at 550 °C/0.001 s⁻¹ and 550 °C/1 s⁻¹. While under the other conditions, predicted flow stresses is in good agreement with experimental value.

2.5 Double multivariate nonlinear regression (DMNR)

The DMNR constitutive equation consists mainly of flow stress (σ) and influence factor (f). Experimental factor (x_i) is strain, strain rate and temperature. Material factor (y_{1i} and y_{2i}) is the independent and interaction action of experimental factor on flow stress. The influence factor is a function of the experimental factor on the flow stress, and is a parameter linking the strain, strain rate and temperature. The weight factor (w_j) is the relative weight of the influence factor on the independent and interaction action of flow stress. Flow stress is a functional of weight factor and influence factor. The relation between flow stress, experimental parameters and analysis parameters is shown in Fig.14^[30,31].

From the physical theory of plastic deformation, it can be obtained:

Table 4 Coefficients of the polynomial fitting for α , Q , n and $\ln A$

α	Q	n	$\ln A$
$D_0=0.01563$	$F_0=249.787\ 31$	$E_0=8.480\ 76$	$C_0=20.305\ 28$
$D_1=-0.098\ 81$	$F_1=601.836\ 61$	$E_1=-56.494\ 95$	$C_1=212.639\ 79$
$D_2=0.652\ 3$	$F_2=-4\ 023.707\ 75$	$E_2=500.814\ 03$	$C_2=-1\ 880.090\ 35$
$D_3=-2.594\ 78$	$F_3=10\ 582.168\ 06$	$E_3=-2\ 640.630\ 01$	$C_3=8\ 354.175\ 43$
$D_4=6.416\ 78$	$F_4=-11\ 480.249\ 9$	$E_4=8\ 129.263\ 09$	$C_4=-21\ 826.390\ 9$
$D_5=-9.923\ 28$	$F_5=-1\ 790.700\ 82$	$E_5=-14\ 767.279\ 44$	$C_5=34\ 757.801\ 08$
$D_6=9.306\ 23$	$F_6=17\ 007.373\ 49$	$E_6=15\ 579.006\ 94$	$C_6=-32\ 980.056\ 27$
$D_7=-4.826\ 64$	$F_7=-15\ 760.764\ 62$	$E_7=-8\ 819.087\ 3$	$C_7=17\ 061.739\ 9$
$D_8=1.059\ 68$	$F_8=4\ 865.873\ 96$	$E_8=2\ 070.188\ 49$	$C_8=-3\ 693.439\ 98$

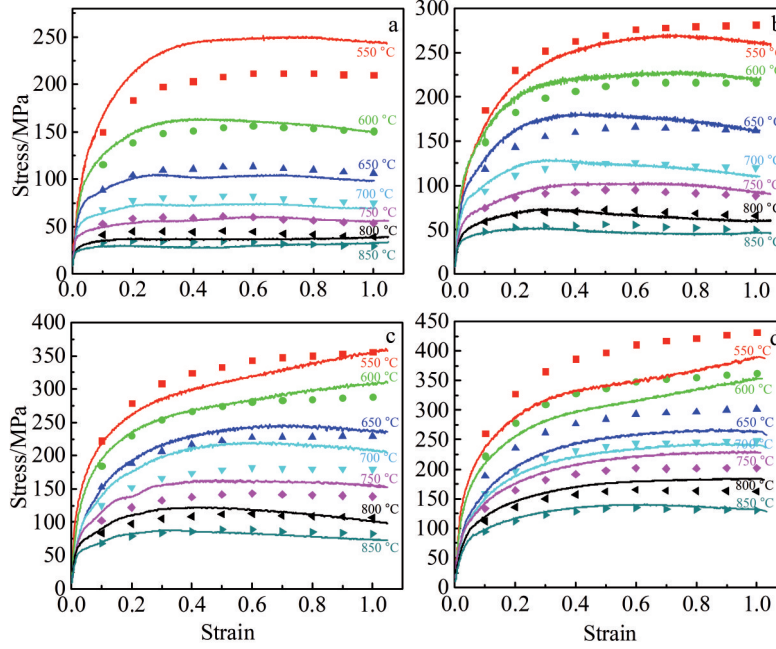


Fig.13 Comparison between experimental and predicted flow stress using MCA model at different strain rates: (a) 0.001 s⁻¹, (b) 0.01 s⁻¹, (c) 0.1 s⁻¹, and (d) 1 s⁻¹

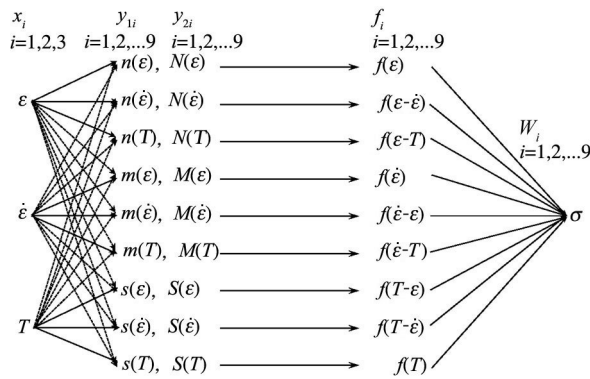


Fig.14 Relation between flow stress, experimental parameters and analytical parameters

$$\sigma = N\epsilon^n \tag{22}$$

$$\sigma = M\dot{\epsilon}^m \tag{23}$$

$$\sigma = S \exp\left(\frac{S}{T}\right) \tag{24}$$

where n, m, s, N, M and S are material parameters. Taking the natural logarithm of both sides of Eq.(22~24):

$$\ln \sigma = \ln N + n \ln \epsilon \tag{25}$$

$$\ln \sigma = \ln M + m \ln \dot{\epsilon} \tag{26}$$

$$\ln \sigma = \ln S + \left(\frac{S}{T}\right) \tag{27}$$

The solving process of the DMNR parameters is shown in Table 5. Firstly, the flow stress of the experimental factor independent and interaction should be calculated. The figure of the relation between experimental factor and flow stress should be drawn, and the slope and intercept can be obtained.

Secondly, the curves of the slope and intercept vs the corresponding experimental factor are fitted to obtain the material factor. Finally, the analysis factor obtained by the function relation is analyzed for regression to predict the flow stress.

The specific solution process is as follows:

In this study, the selected temperatures are 550, 600, 650, 700, 750, 800 and 850 °C. The strain rates are 0.001, 0.01, 0.1 and 1 s⁻¹, and the strain are 0.1, 0.2, 0.3, 0.4, 0.5, 0.6, 0.7, 0.8, 0.9 and 1.0. That is, $K_7=7, K_\epsilon=4$, and $K_\epsilon=10$.

Firstly, the stress values are obtained for all temperature and strain rates at different strain. The relation curve of $\ln \bar{\sigma}(\epsilon) - \ln \epsilon$ is fitted to obtain the intercepts and slopes, that are $\ln N(\epsilon)$ and $n(\epsilon)$, respectively. The intercepts and slopes under different strain are polynomially fitted, as shown in Fig. 15, and the results are as follows:

$$\ln N(\epsilon) = 5.55873 - 0.87036\epsilon - 3.6972\epsilon^2 + 15.79193\epsilon^3 - 20.03616\epsilon^4 + 8.48974\epsilon^5 \tag{28}$$

$$n(\epsilon) = 0.3 + 0.45541\epsilon - 8.22101\epsilon^2 + 23.69677\epsilon^3 - 27.50044\epsilon^4 + 11.33974\epsilon^5 \tag{29}$$

Secondly, the stress values are obtained for all temperatures at different strain and strain rates. The relation curve of $\ln \bar{\sigma}(\epsilon - \dot{\epsilon}) - \ln \dot{\epsilon}$ is fitted to obtain the intercepts and slopes, that are $\ln N(\dot{\epsilon})$ and $n(\dot{\epsilon})$. The intercepts and slopes under different strain rates are polynomially fitted, as shown in Fig. 16, and the results are as follows:

$$\ln N(\dot{\epsilon}) = 5.58034 + 0.01552\dot{\epsilon} - 0.03826\dot{\epsilon}^2 - 0.00303\dot{\epsilon}^3 \tag{30}$$

$$n(\dot{\epsilon}) = 0.19755 + 0.00235\dot{\epsilon} - 0.00804\dot{\epsilon}^2 - 0.000868\dot{\epsilon}^3 \tag{31}$$

Finally, the stress values are obtained for all strain rates at different temperatures. The relation curve of $\ln \bar{\sigma}(\dot{\epsilon} - T) - \ln T$ is fitted to obtain the intercepts and slopes, that are $N(T)$ and $n(T)$. The intercepts and slopes at different temperatures are

Table 5 Solving process of the DMNR parameters

Experimental factor	Formula	Stress	Material factor	Analysis factor	Stress calculation	
ε	$\sigma = N\varepsilon^n$ $\ln\sigma = \ln N + n \ln\varepsilon^n$	$\bar{\sigma}(\varepsilon) = \sum_{T-\dot{\varepsilon}} \sigma(\varepsilon, \dot{\varepsilon}, T) / K_T K_{\dot{\varepsilon}}$	$n(\varepsilon)$	$\ln N(\varepsilon)$	$f_1 = f_{\varepsilon} = N(\varepsilon) \varepsilon^{n(\varepsilon)}$	$\sigma = \sigma_0 \prod_{j=1}^9 f_j^{\omega_j}$
		$\bar{\sigma}(\varepsilon - \dot{\varepsilon}) = \sum_T \sigma(\varepsilon, \dot{\varepsilon}, T) / K_T$	$n(\dot{\varepsilon})$	$\ln N(\dot{\varepsilon})$	$f_2 = f_{\varepsilon - \dot{\varepsilon}} = N(\dot{\varepsilon}) \varepsilon^{n(\dot{\varepsilon})}$	
		$\bar{\sigma}(\varepsilon - T) = \sum_{\dot{\varepsilon}} \sigma(\varepsilon, \dot{\varepsilon}, T) / K_{\dot{\varepsilon}}$	$n(T)$	$\ln N(T)$	$f_3 = f_{\varepsilon - T} = N(T) \varepsilon^{n(T)}$	
$\dot{\varepsilon}$	$\sigma = M\dot{\varepsilon}^m$ $\ln\sigma = \ln M + m \ln\dot{\varepsilon}$	$\bar{\sigma}(\dot{\varepsilon}) = \sum_{\varepsilon-T} \sigma(\varepsilon, \dot{\varepsilon}, T) / K_{\varepsilon} K_T$	$m(\dot{\varepsilon})$	$\ln M(\dot{\varepsilon})$	$f_4 = f_{\dot{\varepsilon}} = M(\dot{\varepsilon}) \varepsilon^{m(\dot{\varepsilon})}$	
		$\bar{\sigma}(\dot{\varepsilon} - \varepsilon) = \sum_T \sigma(\varepsilon, \dot{\varepsilon}, T) / K_T$	$m(\varepsilon)$	$\ln N(\varepsilon)$	$f_5 = f_{\dot{\varepsilon} - \varepsilon} = M(\varepsilon) \varepsilon^{m(\varepsilon)}$	
		$\bar{\sigma}(\dot{\varepsilon} - T) = \sum_{\varepsilon} \sigma(\varepsilon, \dot{\varepsilon}, T) / K_{\varepsilon}$	$m(T)$	$\ln M(T)$	$f_6 = f_{\dot{\varepsilon} - T} = M(T) \varepsilon^{m(T)}$	
T	$\sigma = S \exp(s/T)$ $\ln\sigma = \ln S + s/T$	$\bar{\sigma}(T) = \sum_{\varepsilon-\dot{\varepsilon}} \sigma(\varepsilon, \dot{\varepsilon}, T) / K_{\varepsilon} K_{\dot{\varepsilon}}$	$s(T)$	$\ln S(T)$	$f_7 = f_T = S(T) \exp[s(T)/T]$	
		$\bar{\sigma}(T - \varepsilon) = \sum_{\dot{\varepsilon}} \sigma(\varepsilon, \dot{\varepsilon}, T) / K_{\dot{\varepsilon}}$	$s(\varepsilon)$	$\ln S(\varepsilon)$	$f_8 = f_{T - \varepsilon} = S(\varepsilon) \exp[s(\varepsilon)/T]$	
		$\bar{\sigma}(T - \dot{\varepsilon}) = \sum_{\varepsilon} \sigma(\varepsilon, \dot{\varepsilon}, T) / K_{\varepsilon}$	$s(\dot{\varepsilon})$	$\ln S(\dot{\varepsilon})$	$f_9 = f_{T - \dot{\varepsilon}} = S(\dot{\varepsilon}) \exp[s(\dot{\varepsilon})/T]$	

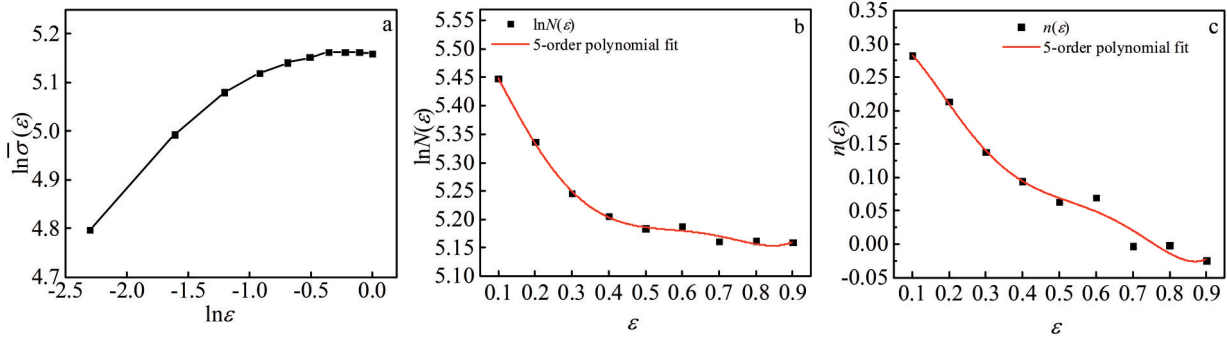


Fig.15 Relation of $\ln\bar{\sigma}(\varepsilon)-\ln\varepsilon$ (a), $\ln N(\varepsilon)-\varepsilon$ (b), and $n(\varepsilon)-\varepsilon$ (c)

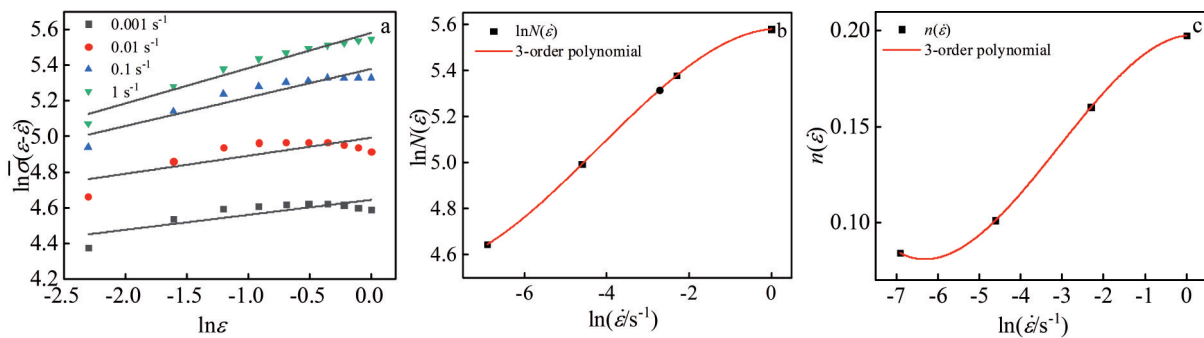


Fig.16 Relation of $\ln\bar{\sigma}(\varepsilon-\dot{\varepsilon})-\ln\varepsilon$ (a), $\ln N(\dot{\varepsilon})-\dot{\varepsilon}$ (b), and $n(\dot{\varepsilon})-\dot{\varepsilon}$ (c)

polynomially fitted, as shown in Fig. 17, and the results are as follows:

$$\ln N(T) = 33.02104 - 8.15333(T/100) + 0.83605(T/100)^2 - 0.03007(T/100)^3 \quad (32)$$

$$n(T) = 39.38192 - 15.43893(T/100) + 2.263(T/100)^2 - 0.14608(T/100)^3 + 0.00349(T/100)^4 \quad (33)$$

Similarly, the $\ln M(\dot{\varepsilon})$ and $m(\dot{\varepsilon})$ are obtained, as shown in Fig.18, where $\ln M(\dot{\varepsilon})=5.48202$, $m(\dot{\varepsilon})=0.1259$.

The $\ln M(\varepsilon)$ and $m(\varepsilon)$ are obtained, as shown in Fig. 19a.

The $\ln M(\varepsilon)$ and $m(\varepsilon)$ under different strain are polynomially fitted, as shown in Fig. 19b and 19c, and the results are as follows:

$$\ln M(\varepsilon) = 4.7888 + 4.11074\varepsilon - 8.78914\varepsilon^2 + 8.55601\varepsilon^3 - 3.0829\varepsilon^4 \quad (34)$$

$$m(\varepsilon) = 0.09457 + 0.08028\varepsilon - 0.02156\varepsilon^2 - 0.05824\varepsilon^3 + 0.04774\varepsilon^4 \quad (35)$$

The $\ln M(T)$ and $m(T)$ are obtained, as shown in Fig. 20a. The $\ln M(T)$ and $m(T)$ at different temperatures are

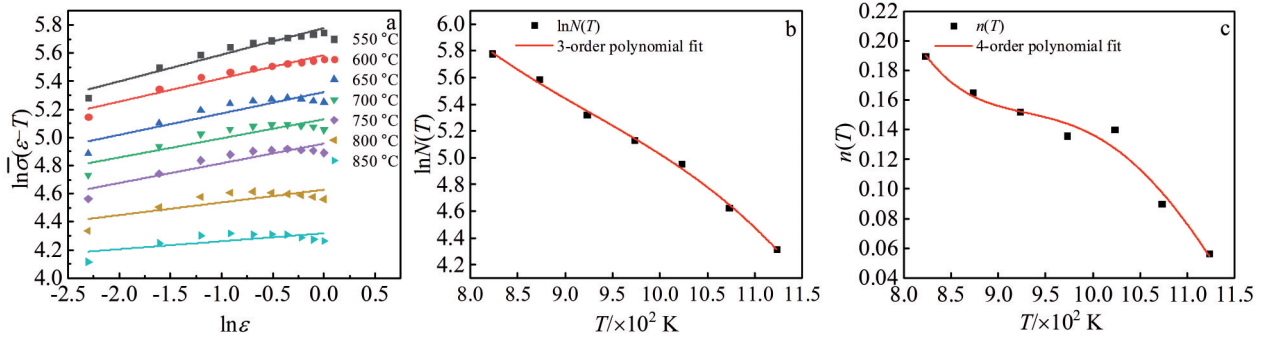


Fig.17 Relation of $\ln\bar{\sigma}(\varepsilon-T)-\ln\varepsilon$ (a), $\ln N(T)-T$ (b), and $n(T)-T$ (c)

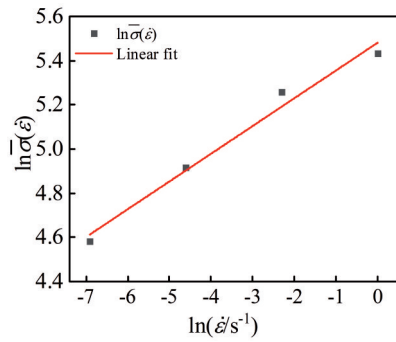


Fig.18 Relation between $\ln\bar{\sigma}(\dot{\varepsilon})$ and $\ln\dot{\varepsilon}$

$$\begin{aligned} \ln M(T) = & -1981.22372 - 9849.45384(T/1000) \\ & -19387.50236(T/1000)^2 \\ & +18943.76653(T/1000)^3 \\ & -9189.08672(T/1000)^4 \\ & +1770.08864(T/1000)^5 \end{aligned} \quad (36)$$

$$\begin{aligned} m(T) = & 428.47695 - 2157.61024(T/1000) \\ & +4316.90653(T/1000)^2 \\ & -4290.79379(T/1000)^3 \\ & +2119.62783(T/1000)^4 \\ & -416.43968(T/1000)^5 \end{aligned} \quad (37)$$

polynomially fitted, as shown in Fig. 20b and 20c, and the results are as follows:

Similarly, the $\ln S(T)$ and $s(T)$ are obtained, as shown in Fig.21, where $\ln S(T)=1.92098$, $s(T)=3.06755$.

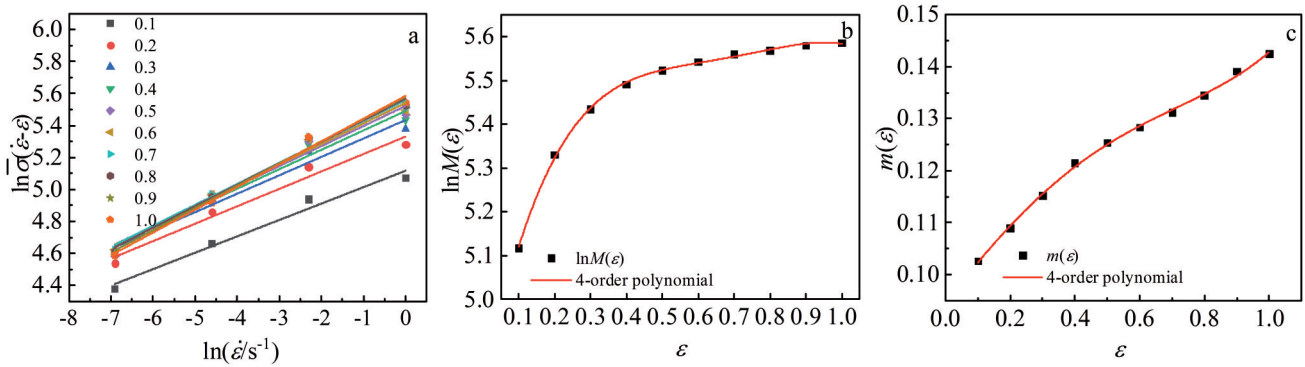


Fig.19 Relation of $\ln\bar{\sigma}(\dot{\varepsilon}-\varepsilon)-\ln\dot{\varepsilon}$ (a), $\ln M(\varepsilon)-\varepsilon$ (b), and $m(\varepsilon)-\varepsilon$ (c)

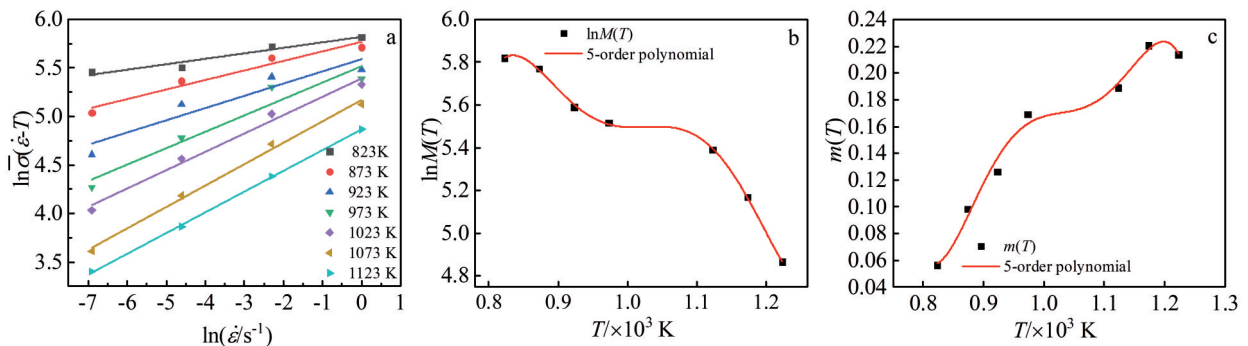


Fig.20 Relation of $\ln\bar{\sigma}(\dot{\varepsilon}-T)-\ln\dot{\varepsilon}$ (a); $\ln M(T)-T$ (b), and $m(T)-T$ (c)

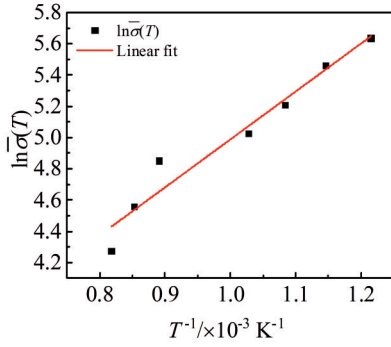


Fig.21 Relation between $\ln\bar{\sigma}(T)$ and $1/T$

The $\ln S(\varepsilon)$ and $s(\varepsilon)$ are obtained, as shown in Fig.22a. The $\ln S(\varepsilon)$ and $s(\varepsilon)$ under different strain are polynomially fitted, as shown in Fig. 22b and 22c, and the results are as follows:

$$\ln S(\varepsilon) = 1.96258 + 0.73888\varepsilon - 1.60519\varepsilon^2 + 0.52804\varepsilon^3 + 0.07553\varepsilon^4 \quad (38)$$

$$s(\varepsilon) = 2.45502 + 2.98072\varepsilon - 6.74239\varepsilon^2 + 7.74657\varepsilon^3 - 3.11224\varepsilon^4 \quad (39)$$

The $\ln S(\dot{\varepsilon})$ and $s(\dot{\varepsilon})$ are obtained, as shown in Fig.23a. The $\ln S(\dot{\varepsilon})$ and $s(\dot{\varepsilon})$ under different strain rates are polynomially fitted, as shown in Fig. 23b and 23c, and the results are as follows:

$$\ln S(\dot{\varepsilon}) = 3.36683 + 0.54611\dot{\varepsilon} \quad (40)$$

$$s(\dot{\varepsilon}) = 2.02328 - 0.52462\dot{\varepsilon} - 0.04373\dot{\varepsilon}^2 - 0.00361\dot{\varepsilon}^3 \quad (41)$$

Bring these parameters into Eq.(42) to obtain the analysis factor. The expression of constitutive equation of DMNR is

shown as Eq.(43). Take the natural logarithm on both sides of Eq.(43), as shown in Eq.(44). Multiple regression of the $\ln\sigma$ and $\ln f_i$ is analyzed using EXCEL software to obtain the parameters of intercept and weight factor. The solution parameters are shown in Table 6.

$$\begin{aligned} f_1 &= f_\varepsilon = N(\varepsilon)\varepsilon^{n(\varepsilon)} \\ f_2 &= f_{\varepsilon-\dot{\varepsilon}} = N(\dot{\varepsilon})\varepsilon^{n(\dot{\varepsilon})} \\ f_3 &= f_{\varepsilon-T} = N(T)\varepsilon^{n(T)} \\ f_4 &= f_{\dot{\varepsilon}} = M(\dot{\varepsilon})\varepsilon^{m(\dot{\varepsilon})} \\ f_5 &= f_{\dot{\varepsilon}-\varepsilon} = M(\varepsilon)\varepsilon^{m(\varepsilon)} \\ f_6 &= f_{\dot{\varepsilon}-T} = M(T)\varepsilon^{m(T)} \end{aligned} \quad (42)$$

$$\begin{aligned} f_7 &= f_T = S(T)\exp\left[\frac{s(T)}{T}\right] \\ f_8 &= f_{T-\varepsilon} = S(\varepsilon)\exp\left[\frac{s(\varepsilon)}{T}\right] \\ f_9 &= f_{T-\dot{\varepsilon}} = S(\dot{\varepsilon})\exp\left[\frac{s(\dot{\varepsilon})}{T}\right] \\ \sigma &= \sigma(\varepsilon, \dot{\varepsilon}, T) = \sigma_0 f_\varepsilon^{\omega_1} f_{\varepsilon-\dot{\varepsilon}}^{\omega_2} f_{\varepsilon-T}^{\omega_3} f_{\dot{\varepsilon}}^{\omega_4} f_{\dot{\varepsilon}-\varepsilon}^{\omega_5} \\ &\quad f_{\dot{\varepsilon}-T}^{\omega_6} f_T^{\omega_7} f_{T-\varepsilon}^{\omega_8} f_{T-\dot{\varepsilon}}^{\omega_9} \end{aligned} \quad (43)$$

$$\begin{aligned} \ln \sigma &= \ln \sigma_0 + \omega_1 \ln f_\varepsilon + \omega_2 \ln f_{\varepsilon-\dot{\varepsilon}} + \omega_3 \ln f_{\varepsilon-T} + \omega_4 \ln f_{\dot{\varepsilon}} \\ &\quad + \omega_5 \ln f_{\dot{\varepsilon}-\varepsilon} + \omega_6 \ln f_{\dot{\varepsilon}-T} + \omega_7 \ln f_T + \omega_8 \ln f_{T-\varepsilon} \\ &\quad + \omega_9 \ln f_{T-\dot{\varepsilon}} \end{aligned} \quad (44)$$

It is observed from Fig. 24 that the deviation is larger compared with the experimental value at strain rate of 0.001 and 0.01 s^{-1} .

2.6 Modified Inoue Sin (MIS) model

The modified Inoue Sin (MIS) constitutive relation is expressed in Eq.(45):

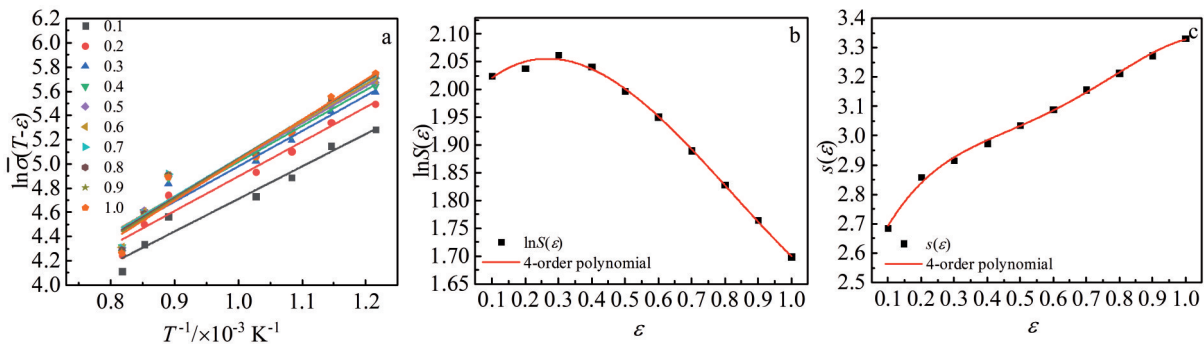


Fig.22 Relation between $\ln\bar{\sigma}(T-\varepsilon)-1/T$ (a), $\ln S(\varepsilon)-\varepsilon$ (b), and $s(\varepsilon)-\varepsilon$ (c)

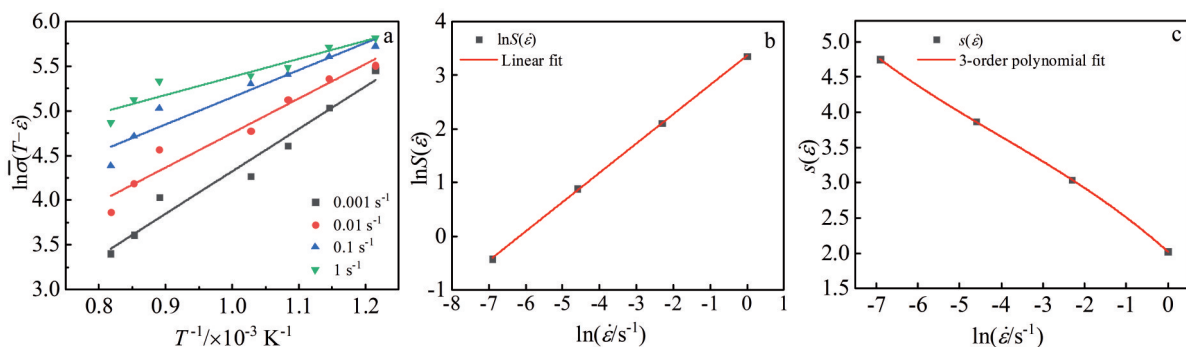


Fig.23 Relation of $\ln\bar{\sigma}(T-\dot{\varepsilon})-1/T$ (a), $\ln S(\dot{\varepsilon})-\dot{\varepsilon}$ (b), and $s(\dot{\varepsilon})-\dot{\varepsilon}$ (c)

Table 6 Parameters of intercept and weight factor

σ_0	ω_1	ω_2	ω_3	ω_4	ω_5	ω_6	ω_7	ω_8	ω_9
2.806 51	- 0.587 64	0.394 49	0.352 44	0.657 35	- 1.084 26	0.589 11	0.264 54	0.438 13	- 0.579 16

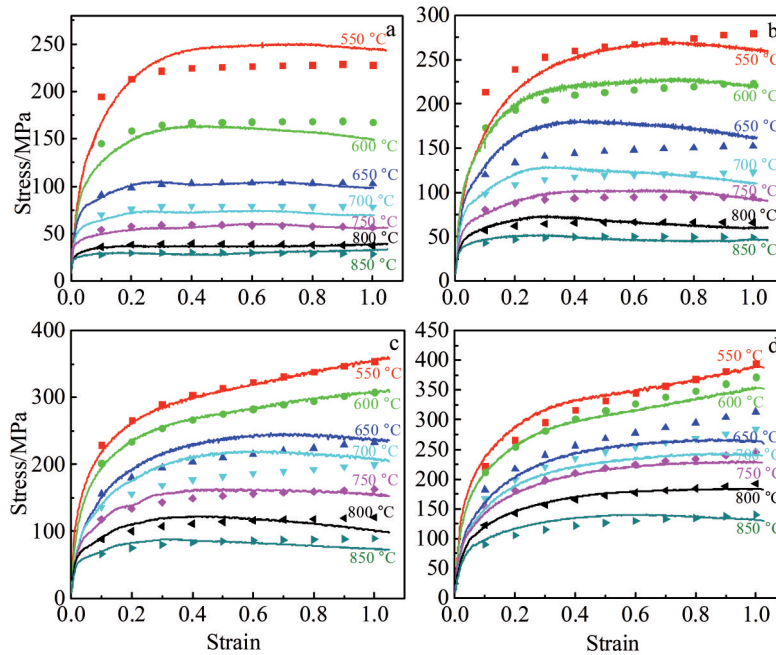


Fig.24 Comparison between experimental and predicted flow stress using DMNR model at different strain rates: (a) 0.001 s⁻¹, (b) 0.01 s⁻¹, (c) 0.1 s⁻¹, and (d) 1 s⁻¹

$$\sigma = a_0 \varepsilon^{a_1 T^2 + bT + c} \dot{\varepsilon}^{a_2 T} \exp\left(\frac{a_3}{T}\right) \quad (45)$$

where b and c are constant. The right side of Eq.(45) can be regarded as strain, strain rate and temperature independent product. Thus, the following equation can be obtained.

$$\frac{\partial \ln \sigma}{\partial \ln \varepsilon} = a_1 T^2 + bT + c \quad (46)$$

$$\frac{\partial \ln \sigma}{\partial \ln \dot{\varepsilon}} = a_2 T \quad (47)$$

$$\frac{\partial \ln \sigma}{\partial \left(\frac{1}{T}\right)} = a_3 \quad (48)$$

The values of $a_1 T^2 + bT + c$ are the slopes after linear fitting for the $\ln \sigma - \ln \varepsilon$ relation at different temperatures and strain rates. Take the strain rate of 0.001 s⁻¹ as an example, as shown in Fig.25a. The values of a_1 , b and c are the constants after the fitting of $a_1 T^2 + bT + c - T$ curves, as shown in Fig.25b. It can be obtained that $a_1 = -3.043 21$, $b = 0.000 12$ and $c = 0.284 81$.

The values of $a_2 T$ and a_3 are the slopes after linear fitting for the $\ln \sigma - \ln \dot{\varepsilon}$ and $\ln \sigma - 1/T$ relation at different temperatures and true strain, respectively. Take the true strain of 0.1 as an example, as shown in Fig.26a and 26b. The value of a_2 and a_3 can be obtained as $a_2 = 0.020 413$, $a_3 = 4537.23$.

According to Eq. (45), the relation of $a_0 - T$ is obtained. Taking the true strain of 0.1 as an example, as shown in Fig.27, it can be seen that the values vary greatly at different strain rates. So, the values of a_0 in segments in this study can be obtained: $a_0 = 40.443 37$ ($\dot{\varepsilon} = 0.001$ s⁻¹), $a_0 = 5.983 53$ ($\dot{\varepsilon} = 0.01$

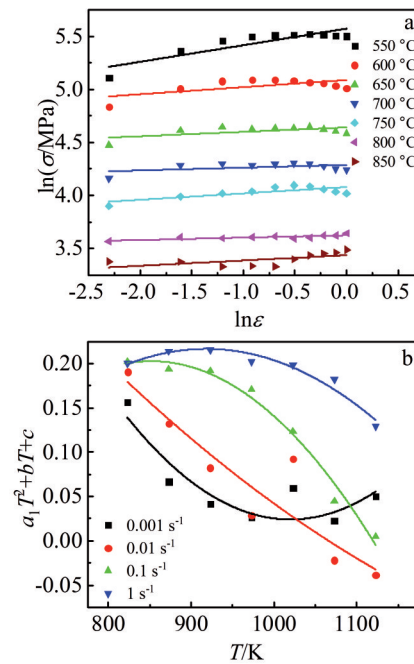


Fig.25 Relation of $\ln \sigma - \ln \varepsilon$ at 0.001 s⁻¹ (a) and relation between $a_1 T^2 + bT + c$ and T (b)

s⁻¹), $a_0 = 0.874 16$ ($\dot{\varepsilon} = 0.1$ s⁻¹), $a_0 = 0.10829$ ($\dot{\varepsilon} = 1$ s⁻¹).

Therefore, the rheological stress of the Ti/Ni/Ti laminated composites is determined in sections as:

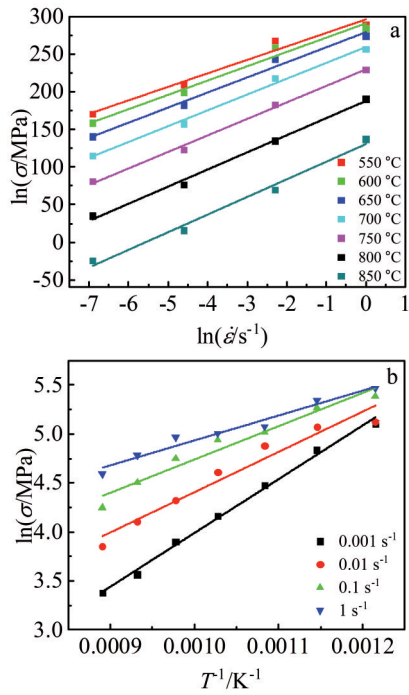


Fig.26 Relation between $\ln\sigma$ - $\ln\dot{\epsilon}$ (a) and $\ln\sigma$ - $1/T$ (b) at strain of 0.1

$$\begin{aligned} \dot{\epsilon} &= 0.001 \text{ s}^{-1}: \\ \sigma &= 40.44337 \epsilon^{-3.04321 \times 10^{-7} T^2 + 0.00012T + 0.28481} \dot{\epsilon}^{0.0204137} \\ &\quad \times \exp\left(\frac{4537.23}{T}\right) \end{aligned} \quad (49)$$

$$\begin{aligned} \dot{\epsilon} &= 0.01 \text{ s}^{-1}: \\ \sigma &= 5.98353 \epsilon^{-3.04321 \times 10^{-7} T^2 + 0.00012T + 0.28481} \dot{\epsilon}^{0.0204137} \\ &\quad \times \exp\left(\frac{4537.23}{T}\right) \end{aligned} \quad (50)$$

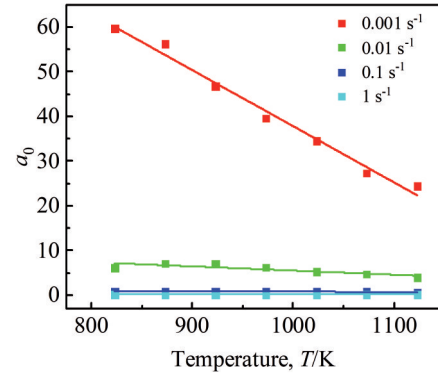


Fig.27 Relation between a_0 and T at strain of 0.1

$$\begin{aligned} \dot{\epsilon} &= 0.1 \text{ s}^{-1}: \\ \sigma &= 0.87416 \epsilon^{-3.04321 \times 10^{-7} T^2 + 0.00012T + 0.28481} \dot{\epsilon}^{0.0204137} \\ &\quad \times \exp\left(\frac{4537.23}{T}\right) \end{aligned} \quad (51)$$

$$\begin{aligned} \dot{\epsilon} &= 1 \text{ s}^{-1}: \\ \sigma &= 0.10829 \epsilon^{-3.04321 \times 10^{-7} T^2 + 0.00012T + 0.28481} \dot{\epsilon}^{0.0204137} \\ &\quad \times \exp\left(\frac{4537.23}{T}\right) \end{aligned} \quad (52)$$

It is observed from Fig. 28 that the deviation is larger compared with the experimental value at strain rate of 0.001 and 0.01 s^{-1} .

3 Discussion

In order to more accurately measure the consistency of the constitutive equation and the test data, the correlation coefficient (R), average absolute relative error (AARE) and relative error are introduced for the error analysis, and the

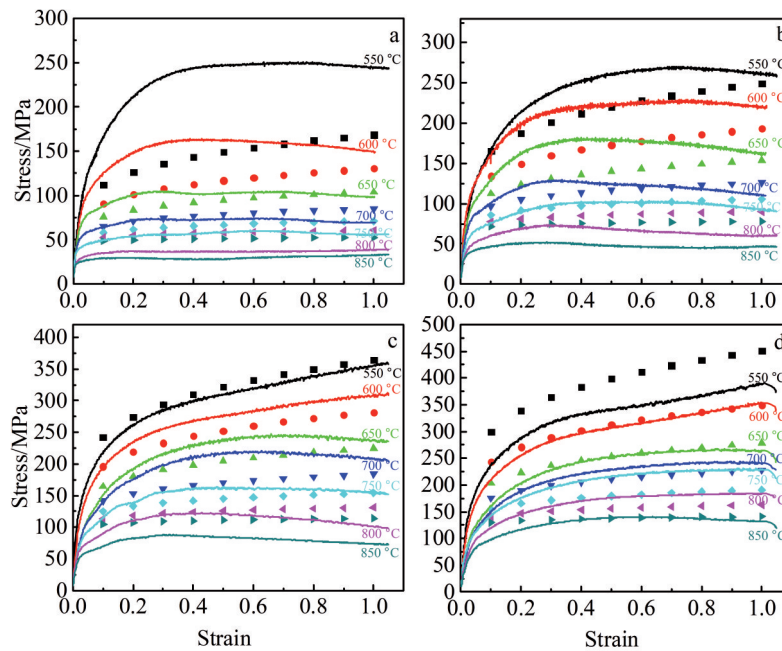


Fig.28 Comparison between experimental and predicted flow stress by MIS model at different strain rates: (a) 0.001 s^{-1} , (b) 0.01 s^{-1} , (c) 0.1 s^{-1} , and (d) 1 s^{-1}

expression is as follows^[32]:

$$R = \frac{\sum_{i=1}^N (E_i - \bar{E})(P_i - \bar{P})}{\sqrt{\sum_{i=1}^N (E_i - \bar{E})^2 \sum_{i=1}^N (P_i - \bar{P})^2}} \quad (53)$$

$$AARE = \frac{1}{N} \sum_{i=1}^N \left| \frac{E_i - P_i}{E_i} \right| \times 100\% \quad (54)$$

where E_i is the test stress value (MPa); \bar{E} is the average value of test stress (MPa); P_i is the calculated stress value (MPa); \bar{P}

is the calculated average value of flow stress (MPa); N is the number of collected data.

Fig. 29 shows the comparison between experimental and predicted stress by the four constitutive models. It can be seen that the values of R for MJC, SCA, DMNR and MIS models are 0.9810, 0.9822, 0.9568 and 0.9426, respectively. Meanwhile, the values of AARE for MJC, SCA, DMNR and MIS model are 10.66%, 8.10%, 14.76% and 19.29%, respectively. The AARE value of SCA model is the lowest (8.10%), followed by MJC (10.66%), DMNR (14.76%) and MIS

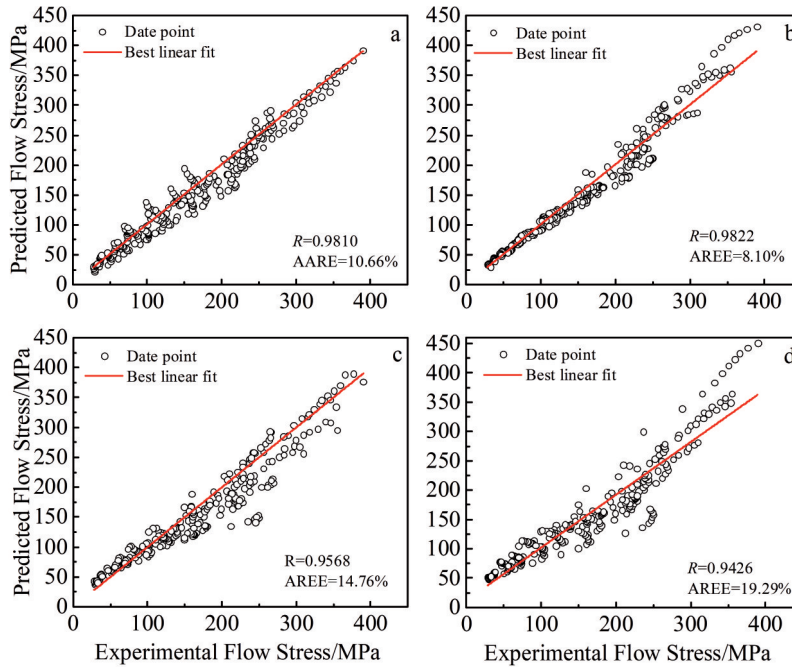


Fig.29 Correlation between the experimental and predicted flow stress values: (a) MJC, (b) SCA, (c) DMNR, and (d) MIS

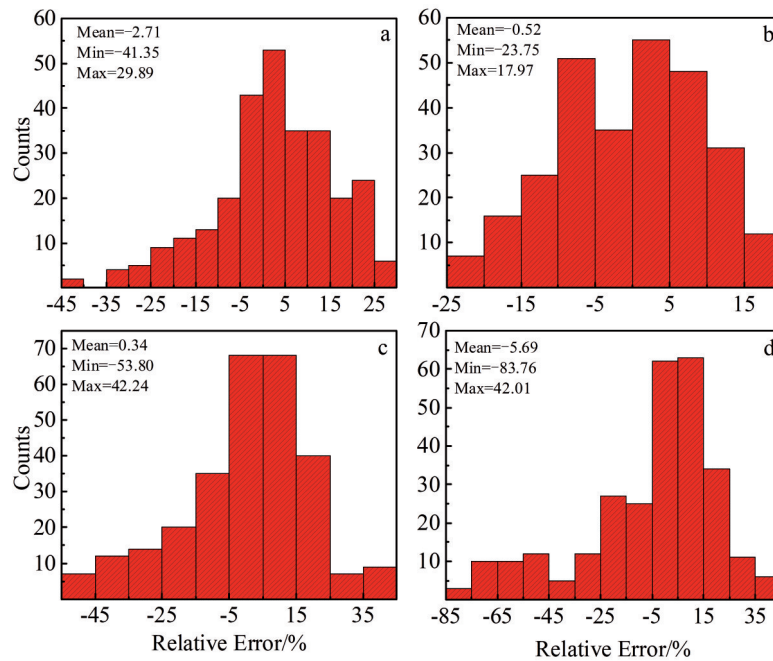


Fig.30 Statistical analysis of the relative error: (a) MJC, (b) SCA, (c) DMNR, and (d) MIS

(19.29%). In addition, the R value of SCA model is the highest (0.9822), followed by MJC (0.9810), DMNR (0.9568) and MIS (0.9426). Therefore, SCA model exhibits the highest accuracy, which indicates that SCA model is more suitable than other models to describe the high temperature flow stress of Ti/Ni/Ti laminated composites.

In order to further analyze the effectiveness of each constitutive model, the relative error is used to analyze the effectiveness of the constitutive model:

$$\text{Relative Error} = \left(\frac{E_i - P_i}{E_i} \right) \times 100\% \quad (55)$$

Fig. 30 shows the relative error comparison of different constitutive models. It can be seen that most of the relative errors of SCA model are in the range of $-10\% \sim 10\%$, while the relative error of MJC, DMNR and MIS models is relatively scattered. For SCA model, there are 190 relative error data located between -10% and 10% , that is 151 for MJC model, 132 for DMNR model, and 107 for MIS model, indicating that SCA model has the most accurate data. In addition, the average, min and max relative errors for SCA model are -0.52 , -23.75 and 17.97 , respectively, which are -2.71 , -41.35 and 29.89 , for MJC model, 0.34 , -53.80 and 42.24 for DMNR model, and -5.69 , -83.76 and 42.01 for MIS model. Therefore, in the whole deformation temperature range, the SCA model is more suitable than other models to describe the high temperature flow stress of Ti/Ni/Ti laminated composites.

4 Conclusions

1) The MJC, DMNR and MIS model are not suitable to predict the elevated temperature flow stress of Ti/Ni/Ti laminated composites over the entire range of strain rates and temperatures, while SCA model can be applied to estimate the flow stress of Ti/Ni/Ti laminated composites at elevated temperatures.

2) The estimation of four constitutive equation models shows that the correlation coefficient (R) for MJC, SCA, DMNR and MIS models is 0.9810, 0.9822, 0.9568 and 0.9426, respectively, while the values of average absolute relative error (AARE) for MJC, SCA, DMNR and MIS model are 10.66%, 8.10%, 14.76% and 19.29%, respectively. It indicates that the SCA model can more accurately predict the elevated temperature flow stress in the entire deformation conditions.

3) All of these results obtained from four kinds of models have some deviation in some deformation conditions, the major reasons may be that the deformation behavior of the material is nonlinear at elevated temperatures and strain rates.

References

- Zhang Youjing, Cheng Xingwang, Cai Hongnian. *Materials & Design*[J], 2016, 92: 486
- Hu Lifang, Xue Yongzhi, Shi Fangrong. *Materials & Design*[J], 2017, 130: 175
- Li Hongying, Li Yanghua, Wei Dongdong et al. *Materials Science and Engineering*[J], 2011, 530: 367
- Changizian P, Zarei-Hanzaki A, Roostaei Ali A. *Materials & Design*[J], 2012, 39: 384
- Wang Qingjuan, Li Xiangjun, Wang Kuaishe et al. *Advanced Engineering Materials*[J], 2019: 22(2): 1 900 772
- Zhou Xuan, Wang Kelu, Lu Shiqiang et al. *Journal of Materials Research and Technology*[J], 2020, 9(3): 2652
- Yang Qunying, Liu Xiaoyong, Liu Guodong et al. *Materials Transactions*[J], 2020, 61(7): 1414
- Niu Yanxia, Hou Jian, Ning Fangkun et al. *Journal of Rare Earths*[J], 2020, 38(6): 665
- Huang Zhiye, Zhang Xingxing, Xiao Bolyu et al. *Journal of Alloys & Compounds*[J], 2017, 722(25): 145
- Zhou Li, Li Ming, Wang Zhaoquan et al. *Acta Metallurgica Sinica*[J], 2020, 56(8): 1155
- Bobbili R, Madhu V J M L. *Materials Letters*[J], 2018, 218: 103
- He Jianli, Chen Fei, Wang Bo et al. *Materials Science and Engineering A*[J], 2017, 715(7): 1
- Abbasi-Bani A, Zarei-Hanzaki A, Pishbin M H et al. *Mechanics of Materials*[J], 2014, 71: 52
- Lin Y C, Chen Xiaomin. *Materials & Design*[J], 2011, 32(4): 1733
- Geng Peihao, Qin Guoliang, Zhou Jun et al. *Journal of Manufacturing Processes*[J], 2018, 32: 469
- Lin Y C, Chen Mingsong, Zhong Jue. *Computational Materials Science*[J], 2008, 42(3): 470
- Tan Y B, Ma Y H, Zhao F. *Journal of Alloys and Compounds*[J], 2018, 741: 85
- Jiang Zhengyi, Gao Xingjian, Li Shengli et al. *Journal of Iron and Steel Research, International*[J], 2015, 22(5): 138
- Hou Qingyu, Wang Taojing. *Computational Materials Science* [J], 2011, 50(1): 147
- Zhao Yanhua, Sun Jie, Li Jianfeng. *Journal of Alloys and Compounds*[J], 2017, 723: 179
- Li Hongying, Li Yanghua, Wang Xiaofeng et al. *Materials & Design*[J], 2013, 49: 493
- Zhang Yi, Sun Huili, Volinsky Alex A et al. *Vacuum*[J], 2017, 146: 35
- Samantaray D, Mandal S, Bhaduri A K. *Computational Materials Science*[J], 2009, 47: 568
- Zhang Cunsheng, Ding Jie, Dong Yuanyuan. *International Journal of Mechanical Sciences*[J], 2015, 98: 195
- Chen Gang, Chen Wei, Ma Li. *Rare Metal Materials and Engineering*[J], 2015, 44(9): 2120
- Li Yufei, Wang Zhenhong, Zhang Linying et al. *Transactions of Nonferrous Metals Society of China*[J], 2015, 25(6): 1889
- Razmpoosh M H, Zarei-Hanzaki A, Imandoust A. *Materials Science & Engineering A*[J], 2015, 638: 15
- Mandal S, Rakesh V, Sivaprasad P V et al. *Materials Science & Engineering A*[J], 2009, 500(1-2): 114

- 29 Wang Kuaishe, Han Yingying, Cai Jun. *High Temperature Materials and Processes*[J], 2016, 35(3): 297
- 30 Yuan Zhanwei, Li Fuguo, Qiao Huijuan et al. *Materials Science and Engineering A*[J], 2013, 578: 260
- 31 Li Pan, Li Fuguo, Cao Jun et al. *Transactions of Nonferrous Metals Society of China*[J], 2016, 26(4): 1079
- 32 Cai Jun, Wang Kuaishe, Zhai Peng et al. *Journal of Materials Engineering and Performance*[J], 2015, 24(1): 32

Ti/Ni/Ti层状复合材料热压缩流动应力预测

赵田丽¹, 张兵^{1,2}, 张志娟¹, 马艳恒¹, 党晓晗¹, 蔡军^{1,2}

(1. 西安建筑科技大学 冶金工程学院, 陕西 西安 710055)

(2. 功能材料加工国家地方联合工程研究中心, 陕西 西安 710055)

摘要: 为了建立合理的能够描述Ti/Ni/Ti层状复合过程的本构方程, 在Gleeble-3500热机械模拟机上对Ti/Ni/Ti层状复合材料在变形温度为550~850 °C, 应变速率为0.001~1 s⁻¹, 变形量为65%的复合过程中热变形行为进行研究。采用4种本构模型: 改进的Johnson-Cook (MJC) 模型、应变补偿Arrhenius (SCA) 模型、多元非线性回归 (DMNR) 模型和改进的井上胜郎 (MIS) 模型对层状复合材料的高温流变行为进行预测。同时, 对4种模型的实验值和预测值进行了比较。此外, 比较了平均绝对相对误差 (AARE)、相关系数 (R) 和相对误差的准确性, 以确定这4种模型的合理性。结果表明, MJC、DMNR和MIS模型都不适合描述Ti/Ni/Ti层状复合材料的流变行为, 而SCA模型除了在某些特定变形条件外, 其预测值与实验值吻合较好。

关键词: Ti/Ni/Ti层状复合材料; 热压缩; 流动应力; 本构方程

作者简介: 赵田丽, 女, 1986年生, 博士, 西安建筑科技大学冶金工程学院, 陕西 西安 710055, E-mail: 394405069@qq.com